Slomka looks at the significance of SPECT-derived quantitative assessment of changes in myocardial perfusion over time and, specifically, after therapy and previews an innovative approach reported in this month's *JNM*. . . . . ***Page 1978***

Itti and colleagues report on voxel-based automated myocardial perfusion scintigraphy quantification methods that more accurately assess change after myocardial infarction and therapy. . . . . ***Page 1981***

Okumura and colleagues investigate the relative usefulness of fasting ^{18}F-FDG PET in detecting inflammatory lesions of early-stage cardiac sarcoidosis. . . . . ***Page 1989***

Abidov and colleagues derive and validate the normal threshold for automatically measured left ventricular transient ischemic dilation ratios in patients referred for adenosine stress myocardial perfusion SPECT and consider the integration of these data into routine assessment of coronary artery disease. . . . . ***Page 1999***

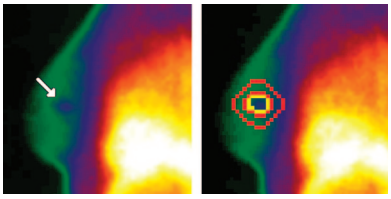

Lubberink and colleagues compare the quantitative accuracy of iteratively reconstructed cardiac ^{18}F-FDG PET with that of filtered backprojection for both 2- and 3-dimensional acquisitions to establish an optimal procedure for PET imaging of myocardial viability. . . . . ***Page 2008***

Schaefer and colleagues contrast a range of prone and supine patient positioning values acquired during gated ^{99m}Tc-myocardial SPECT and discuss the implications for comparing such values with standard reference data. . . . . ***Page 2016***

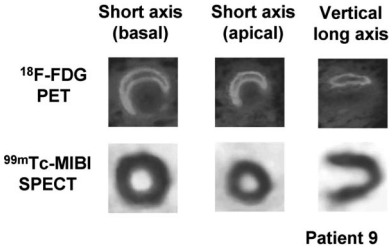

Oommen and colleagues assess the use of specific patterns identified on interictal and postictal SPECT to improve localization of epileptogenic foci in the temporal lobe. . . . . ***Page 2021***

El Fakhri and colleagues look at the beneficial effects of improved quantitative image reconstruction with compensation for scatter, attenuation, and variable collimator response on reader performance in discrimination tasks related to the diagnosis of prodromal Alzheimer's disease. . . . . ***Page 2026***

Roivainen and colleagues report on metabolism and whole-body distribution of intravenously administered ^{11}C-MP4B, a new radiopharmaceutical for PET assessment of butyrylcholinesterase activity. . . . . ***Page 2032***

Wilczek and colleagues compare the abilities of ^{99m}Tc-exametazime with those of ^{99m}Tc-sestamibi as mammoscintigraphic tumor-imaging radiopharmaceuticals. . . . . ***Page 2040***

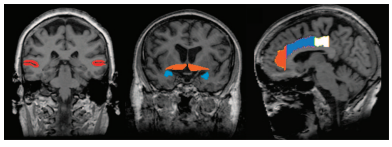

Israel and colleagues evaluate the incremental role of ^{18}F-FDG PET/CT in the diagnosis and management of cancer patients with increasing levels of tumor markers as the sole indicator of potential recurrence after initial successful treatment. . . . . ***Page 2045***

de Boer and colleagues assess whether quantitative ^{11}C-TYR PET has predictive value for survival and therapy outcome in patients with primary squamous cell carcinoma of the larynx. . . . . ***Page 2052***

Kumar and colleagues report on the role and additional benefits of ^{18}F-FDG PET in differentiating benign from metastatic adrenal masses detected on CT or MRI in patients with lung cancer. . . ***Page 2058***

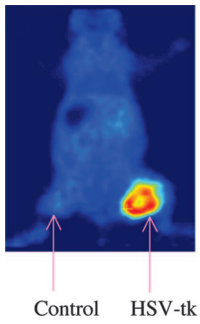

Alauddin and colleagues investigate the biodistribution and uptake characteristics of ^{18}F-FFAU, a potentially superior PET agent for HSV1-tk gene expression imaging. . . . . ***Page 2063***

Tian and colleagues describe the detection of cancer gene activity from outside the body by probing with radionuclide-chelator-peptic nucleic acid-peptide chimeras, a technique that could help to avoid unnecessary biopsies. . ***Page 2070***

Takei and colleagues use an experimental model to determine the best timing for detecting apoptosis in vivo with ^{99m}Tc-annexin V after chemotherapy. . . . . ***Page 2083***

Siaens and colleagues assess differences and similarities in 2 labeled quinolones, ^{99m}Tc-ciprofloxacin and ^{99m}Tc-enrofloxacin, as tracers for infection and inflammation in animals. . . . . ***Page 2088***

Hatada and colleagues report on the myocardial uptake and clearance kinetics ^{99m}Tc-N-DBODC5, a new myocardial perfusion tracer with superior biodistribution properties that promise to markedly reduce photon scatter problems in myocardial images. . . . . ***Page 2095***

Zanzonico and colleagues investigate the effects of continuing antithyroid drugs at a reduced dosage during ^{131}I therapy to reduce extrathyroid radiation without significantly reducing the target tissue dose. . . . . ***Page 2102***

Shin and colleagues develop a dual-imaging reporter gene system and examine the correlation between cancer cell number and signals from 2 reporter genes, a method that could be used to evaluate the effects of various therapeutic approaches. . . . ***Page 2109***

Bergmann and colleagues elucidate the tumor cell transport mechanism for a novel ^{18}F-labeled phenylalanine derivative that is presented as a potential PET tracer for imaging of amino acid transport in tumors. . . . . ***Page 2116***

ON THE COVER
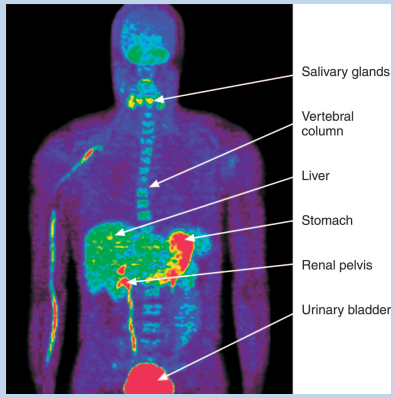
This whole-body PET image of a healthy male volunteer shows that most of the radioactivity is distributed in the urinary bladder, indicating prompt excretion through the renal system. Renal pelvis, stomach, salivary glands, liver, kidneys, spleen, and vertebral column were also clearly visualized. However, uptake in myocardium, pancreas, and lungs was low. The distribution of ^{11}C-MP4B in the brains of patients with Alzheimer's disease appears to be in accordance with the distribution of butyrylcholinesterase seen in postmortem studies of human brain, except for an observed higher activity in striatum than in cortex.